

## Synthesis and Characterization of Uncracked $\text{IrO}_2\text{-SnO}_2\text{-Sb}_2\text{O}_3$ Oxide Films Using Organic Precursors and Their Application for the Oxidation of Tartrazine and Dibenzothiophene

Miguel A. González-Fuentes<sup>1,\*</sup>, Uriel Bruno-Mota<sup>1</sup>, Alia Méndez-Albores<sup>2</sup>, Margarita Teutli-Leon<sup>3</sup>, Alejandro Medel<sup>4</sup>, Ricardo Agustín<sup>5</sup>, Rossy Feria<sup>1</sup>, Adrián A. Hernández<sup>1</sup>, Erika Méndez<sup>1,\*</sup>

<sup>1</sup> Facultad de Ciencias Químicas, Benemérita Universidad Autónoma de Puebla, 72570, Puebla, México

<sup>2</sup> Centro de Química, ICUAP, Benemérita Universidad Autónoma de Puebla, 72570, Puebla, México

<sup>3</sup> Facultad de Ingeniería, Benemérita Universidad Autónoma de Puebla, 72570, Puebla, México

<sup>4</sup> Centro de Investigación y Desarrollo Tecnológico en Electroquímica, S.C., 76703, Pedro Escobedo, Querétaro, México

<sup>5</sup> Facultad de Ciencias Físico Matemáticas, Benemérita Universidad Autónoma de Puebla, 72570, Puebla, México

\*E-mail: [erika.mendez@correo.buap.mx](mailto:erika.mendez@correo.buap.mx); [miguel.gonzalezfuentes@correo.buap.mx](mailto:miguel.gonzalezfuentes@correo.buap.mx)

Received: 24 November 2020 / Accepted: 9 January 2021 / Published: 31 January 2021

---

A ternary coating film of  $\text{IrO}_2\text{-SnO}_2\text{-Sb}_2\text{O}_3$  on a Ti substrate was prepared by thermal decomposition in an adapted protocol of the Pechini method to obtain DSA type electrodes. The polymeric precursor mixture was prepared with nonchlorinated salts of iridium, tin, and antimony in different molar proportions. Iridium(III) acetylacetonate, tin(II) acetate, and antimony(III) acetate were used in small amounts to obtain compact, thin, and uncracked oxide films with homogeneous texture compared with a commercial film of  $\text{Ti|IrO}_2\text{-SnO}_2\text{-Sb}_2\text{O}_5$ . The polymeric precursor solution was brushed onto a pretreated titanium substrate and calcined at 500 °C to convert the coating into  $\text{IrO}_2\text{-SnO}_2\text{-Sb}_2\text{O}_3$ . Physical and electrochemical characterization was performed by SEM, EDX, DRX, and cyclic voltammetry. The formation of ternary oxides was explained according to redox reaction mechanisms involving decarboxylation and thermal decomposition. Even though the polymeric precursor solution was deposited by brushing, the oxide films was thin and homogeneous ( $3.05 \pm 0.35 \mu\text{m}$  thickness). The DSA electrode performance was tested to evaluate the electrochemical oxidation of tartrazine and dibenzothiophene in aqueous and acetonitrile/water media, respectively. All DSAs demonstrated high effectiveness for the decolorization and mineralization of tartrazine (up to 90% and 70%, respectively), mainly by hydroxyl radicals. On the other hand, dibenzothiophene was converted to both dibenzothiophene sulfoxide and dibenzothiophene sulfone by direct electron transfer.

---

**Keywords:** Dibenzothiophene, DSA type electrodes, nonchlorinated salts, tartrazine,  $\text{Ti|IrO}_2\text{-SnO}_2\text{-Sb}_2\text{O}_3$

## 1. INTRODUCTION

Dimensionally Stable Anodes (DSAs) present high electrocatalytic activity, excellent mechanical stability and durability, versatile manufacturing design, and low cost compared with conventional anodes of Pt, Au, and BDD materials [1, 2]. Due to their high corrosion resistance and high electroactive surface, DSAs were initially developed to catalyze chlorine production [3]. Their use also represents a viable option for the oxidation of organic pollutants in industrial effluents [4]. These electrodes are typically manufactured by creating a film of crystalline transition metal oxides onto a titanium substrate or its alloys. The most commonly used oxides include RuO<sub>2</sub>, IrO<sub>2</sub>, TiO<sub>2</sub>, Ta<sub>2</sub>O<sub>5</sub>, SnO<sub>2</sub>, PbO<sub>2</sub>, Sb<sub>2</sub>O<sub>5</sub>, MnO<sub>2</sub>, and some mixtures, such as RuO<sub>2</sub>-SnO<sub>2</sub>, IrO<sub>2</sub>-RuO<sub>2</sub>, RuO<sub>2</sub>-IrO<sub>2</sub>-TiO<sub>2</sub>, and IrO<sub>2</sub>-TiO<sub>2</sub> [5, 6]. Among the mentioned oxides, iridium, tin, and antimony oxides present remarkable properties that make them excellent choices for the preparation of DSAs. IrO<sub>2</sub> provides electrocatalytic properties for chlorine production and promotes the oxygen evolution reaction (OER) [7]. SnO<sub>2</sub> confers a low resistivity and good stability to electrodes, thus representing an excellent alternative for the removal of organic compounds in wastewater [5, 8]. On the other hand, antimony-doped electrodes (Ti|Sb-SnO<sub>2</sub>) are one of the most promising DSA anodes due to their low cost compared with those made of Ti|IrO<sub>2</sub>. These electrodes show a higher oxygen evolution overpotential than IrO<sub>2</sub> and RuO<sub>2</sub> electrodes; however, their main benefit is their long operational lifetime in anodic polarization conditions [2]. Thus, the incorporation of Sb as a dopant has been reported to improve electrical conductivity, mechanical stability, and service lifetime and to confer a high overpotential for the OER [5].

Synthesis conditions such as temperature, pH, and current density strongly influence the physicochemical and electrical properties of DSA films. These properties also depend on the preparation method, calcination temperature, nature of the polymeric precursor solution, and metallic precursor proportion. Selected conditions for each one allow oxides with different crystalline features, thicknesses, electrical conductivities, and surface morphologies to be obtained [9, 10]. The electrocatalytic oxides mixed with stabilizing components are deposited to form DSAs mainly by coating methods such as thermal decomposition, immersion, spray pyrolysis, reactive sputtering, magnetic induction, and induction heating techniques [11–13]. Recently, an adapted Pechini method of preparing DSAs by a thermal method using small amounts of polymeric precursors was published [11]. However, the resulting surfaces showed compact and cracked morphologies. In this regard, some authors have proposed that the morphology of oxide films is directly influenced by the coating technique [14].

On the other hand, other authors suggest that the Pechini method yields cracked films due to the calcination temperature [15, 16]. In this sense, several studies have shown that Ti|IrO<sub>2</sub> electrodes prepared by this method exhibit a longer lifetime due to their higher resistance to corrosion than those prepared by sol-gel or thermal decomposition methods [9, 10]. In the Pechini method, a polyesterification reaction with polyalcohols is necessary to form a chelate between the metallic cation and the carboxylic group [5, 17]. In this step, inorganic precursors derived from metallic chlorides are commonly employed [18–20]. However, during electrode preparation, chlorides can produce undesirably chlorinated byproducts and toxic vapors. These facts provide a considerable disadvantage concerning any selected method.

Considering the complementary properties of the Ir, Sn, and Sb oxides discussed above, in this work, IrO<sub>2</sub>–SnO<sub>2</sub>–Sb<sub>2</sub>O<sub>3</sub> film coatings supported on titanium substrates were synthesized by following an adapted Pechini method. To prevent chlorine vapor emissions to the environment during electrode preparation, nonchlorinated metallic precursors (1) iridium(III) acetylacetonate, (2) tin(II) acetate, and (3) antimony(III) acetate were used, and their molecular structures are shown in Figure 1. The aim was to synthesize and characterize DSAs made from organic precursors of Ir, Sn, and Sb to obtain oxide films with an uncracked morphology. The performance of the synthesized DSAs was evaluated through the oxidation of two common organic pollutants in the food and petroleum industries, (4) tartrazine (TRZ, C<sub>16</sub>H<sub>9</sub>N<sub>4</sub>O<sub>9</sub>S<sub>2</sub>Na<sub>3</sub>) and (5) dibenzothiophene (DBT, C<sub>12</sub>H<sub>8</sub>S), whose chemical structures are shown in Figure 1.

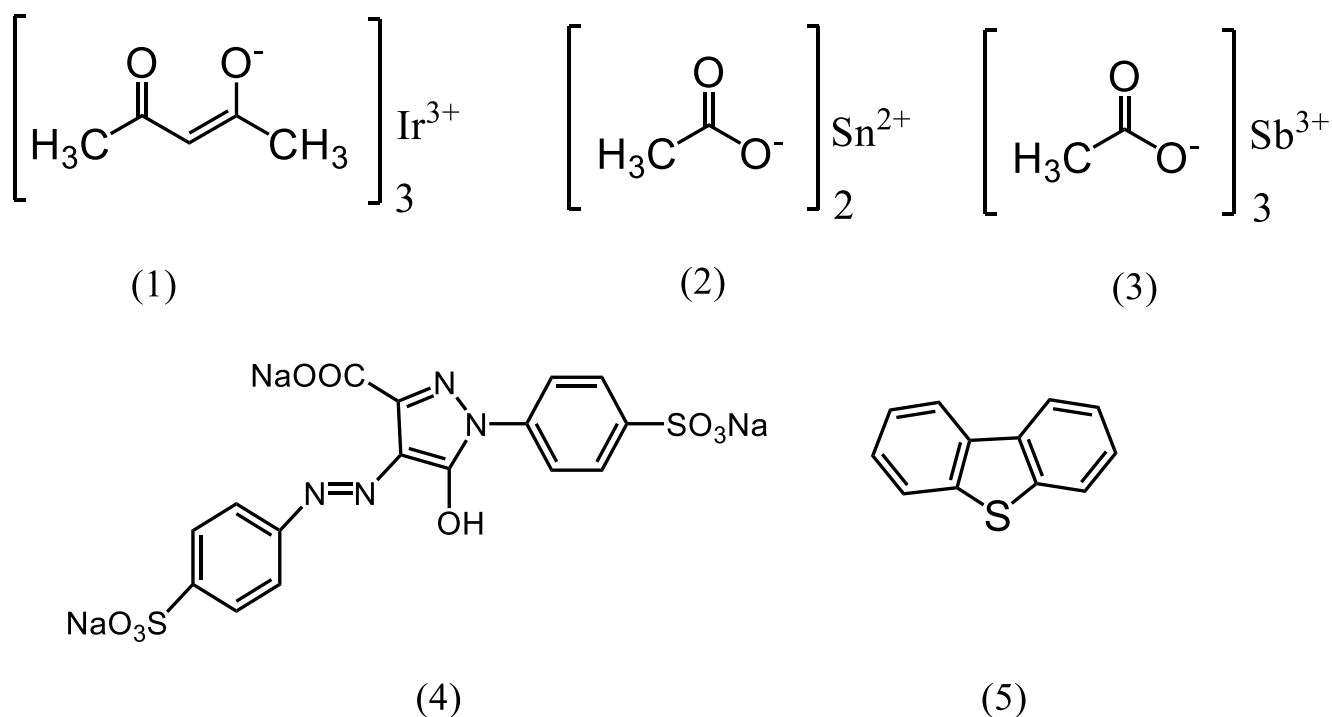


**Figure 1.** Chemical structure of (1) iridium(III) acetylacetonate, (2) tin(II) acetate, (3) antimony(III) acetate, (4) tartrazine, and (5) dibenzothiophene.

## 2. EXPERIMENTAL

### 2.1 Chemicals

Iridium(III) acetylacetonate (97%), tin(II) acetate (99%), antimony(III) acetate (99.9%), ethylene glycol (>99%), Na<sub>2</sub>SO<sub>4</sub> (ACS reagent, >99.0%) citric acid (>99.5%), coumarin (>98%), tartrazine (>85%), dibenzothiophene (98%), HNO<sub>3</sub> (70%) and HClO<sub>4</sub> (70%) were purchased from Sigma–Aldrich. HCl (36.5–38%) and H<sub>2</sub>SO<sub>4</sub> (95.0–98%) were obtained from J.T. Baker. Finally, acetonitrile was procured from Fermont. These chemicals were used without further purification.

## 2.2 Synthesis of Ti/IrO<sub>2</sub>-SnO<sub>2</sub>-Sb<sub>2</sub>O<sub>3</sub> DSAs

### 2.2.1 Surface coating

DSAs were prepared by following a variation of the Pechini method that involves the formation of an organic polyester through metallic citrate polymerization in ethylene glycol [12]. Ternary oxides of SnO<sub>2</sub>, IrO<sub>2</sub>, and Sb<sub>2</sub>O<sub>3</sub> were obtained by thermal decomposition using the corresponding metallic precursor. Sets of DSAs were synthesized starting from 10 ml of a solution of ethylene glycol with 0.12 M citric acid and dissolving different concentration relationships of organic precursors: solution-1 (89:89:2); solution-2 (89:178:2); and solution-3 (178:89:2). Following this precursor solution nomenclature, the synthesized electrodes were named DSA-1, DSA-2 and DSA-3. The numbers in parentheses are millimolar concentrations of compounds **1**, **2**, and **3**. In this sense, the tin(II) acetate concentration was twice as large in DSA-2 than in DSA-1, while the iridium(III) acetylacetonate concentration was two times larger in DSA-3 than in DSA-1 and DSA-2. In all polymeric precursor solutions, the antimony(III) acetate amount was maintained as a constant to analyze the influence of Ir and Sn composition on the electrode properties. Antimony was used to increase the electrode service lifetime and prevent passive external layer formation [21]. The manufacturing procedure used to obtain DSAs with an adapted protocol of the Pechini method has been previously reported [11]; however, in this work, all reagents were mixed simultaneously in ethylene glycol with citric acid and heated to 110 °C. Before coating, Ti mesh substrates were sand polished and then washed with deionized water in an ultrasonic bath for 5 min. After that, the Ti substrates were chemically pretreated with HCl (1.5 h at 70 °C) and HNO<sub>3</sub> (5 min. at 70 °C) to obtain a high surface roughness. These substrates were rinsed three times with boiled deionized water (~90 °C) before applying each polymeric precursor by brushing. Afterward, the electrodes were heated in a furnace at 100 °C for 15 min (this procedure was repeated 32 times) to polymerize the coating and evaporate the solvents. After every four applications, the electrodes were calcined for an hour under atmospheric air at 500 °C in a furnace. Before each electrochemical characterization and use, the surface of the electrodes was activated by imposing a constant potential of -0.1 V/SCE for 5 minutes in either 1 M HClO<sub>4</sub> or 0.5 M H<sub>2</sub>SO<sub>4</sub>.

### 2.2.2 Physical and electrochemical characterization

The microstructure, distribution, composition, and thickness of the metal oxide films formed on the electrode surface were analyzed by scanning electron microscopy (SEM) and energy dispersive X-ray (EDX) techniques with a JEOL JSM-6610LV instrument operated at 20 kV in secondary electron imaging mode coupled to an OXFORD INCAx-act analytical system. For these analyses, the substrates were embedded in Bakelite and cut transversely. The crystal phases of the different metal oxides in the DSA coatings were analyzed by beam X-ray diffraction (XRD) with a BRUKER D8DISCOVER diffractometer using Cu K $\alpha$  radiation, and XRD data were collected for 2 $\theta$  angles between 20° and 80°.

Electrochemical characterization of DSAs was performed using a 302N potentiostat/galvanostat (AUTOLAB) connected to a typical three-electrode cell. The reference and auxiliary electrodes were a saturated calomel electrode and a Pt wire, respectively, whereas the synthesized DSA substrate was the

working electrode. The oxygen evolution overpotential was analyzed by performing linear sweep voltammetry (LSV) at  $0.1 \text{ V s}^{-1}$  in  $1 \text{ M HClO}_4$ , which acted as the supporting electrolyte, whereas the real area of each DSA electrode was evaluated by performing cyclic voltammetry (CV) in  $0.5 \text{ M H}_2\text{SO}_4$  by measuring the current in the capacitive region at different scan rates ( $0.02$  to  $0.1 \text{ V s}^{-1}$ ) [22]. All the solutions were purged by nitrogen bubbling before and during each experimental run at room temperature ( $\sim 25 \text{ }^\circ\text{C}$ ).

Hydroxyl radical ( $\bullet\text{OH}$ ) production was identified indirectly by measuring the decrease in coumarin concentration due to its reaction with hydroxyl radicals, producing 7-hydroxycoumarin [23]. Electrolysis was carried out in a  $0.1 \text{ M Na}_2\text{SO}_4 + 0.1 \text{ mM coumarin}$  solution by applying a  $8 \text{ mA cm}^{-2}$  current density for 20 minutes. Absorption spectra of coumarin and its product (7-hydroxycoumarin) were monitored using a Perkin Elmer spectrophotometer and Cary Eclipse Agilent fluorescence spectrophotometer, respectively.

### 2.3 Oxidation of tartrazine and dibenzothiophene

Exhaustive electrolysis of tartrazine (TRZ, **4**) and dibenzothiophene (DBT, **5**) was accomplished under galvanostatic and potentiostatic regimes, respectively, at room temperature. The anode consisted of the synthesized DSAs, and a Pt mesh served as the cathode and was placed in a salt bridge filled with the corresponding supporting electrolyte in a divided electrochemical cell. The galvanostatic oxidation of  $40 \text{ ppm TRZ}$  dissolved in deionized water +  $0.1 \text{ M Na}_2\text{SO}_4$  was carried out for 2 h by imposing a  $8 \text{ mA cm}^{-2}$  current density with an EZ/GP-1303DU power supply. The oxidation of  $200 \text{ ppm DBT}$  was carried out by applying a  $1.8 \text{ V vs. SCE}$  potential for 90 min in an acetonitrile/water mixture (75:15%) containing  $0.1 \text{ M NEt}_4\text{BF}_4$  as the supporting electrolyte. The potential value of  $1.8 \text{ V}$  was selected from a previous cyclic voltammetry analysis of DBT oxidation. After electrolysis, the organic pollutant consumption was observed *in situ* by performing CV on a glassy carbon electrode. Tartrazine decolorization was also monitored by UV-vis spectrometry (220–700 nm) using a Spelec (DROPSSENS) spectrometer. TRZ mineralization was analyzed by performing total organic carbon measurements with a TOC-LN (SHIMADZU) analyzer. Additionally, byproducts were analyzed by HPLC-MS-TOF using an Agilent system comprising an HPLC 1100 chromatograph equipped with a mass spectrometer (MS-TOF) in ESI (electrospray ionization) mode. The electrolyzed solution of tartrazine was evaporated under vacuum in an ECO-1V Hanvapor system, and the electrolyte was removed with ethanol. All procedures and HPLC-MS-TOF analyses were carried out according to the methodology proposed in our previous work [24].

## 3. RESULTS AND DISCUSSION

### 3.1 Surface characterization

Figure 2(a–c) shows the surface morphology of the different prepared DSAs. The images show similar morphology and roughness in all cases. More cavities with significant depths are present in DSAs

than in the pretreated substrate (Figure 2–d). As a result of this pretreatment, the surface presents a homogeneous distribution of cavities, increasing the surface roughness and favoring the later adhesion of the polymeric precursors used to form the ternary metal oxides. It is essential to mention that the thickness of each film was calculated to be  $3.05 \pm 0.35 \mu\text{m}$ . Their morphology did not present cracks or agglomerated cracks (even when observed at different microscopic scales) compared to the oxide film prepared by the Pechini method using precursor salts containing chloride ions [25, 26], as illustrated in Figure 2–e, which corresponds to a commercial  $\text{Ti}|\text{IrO}_2\text{--SnO}_2\text{--Sb}_2\text{O}_5$  DSA electrode.

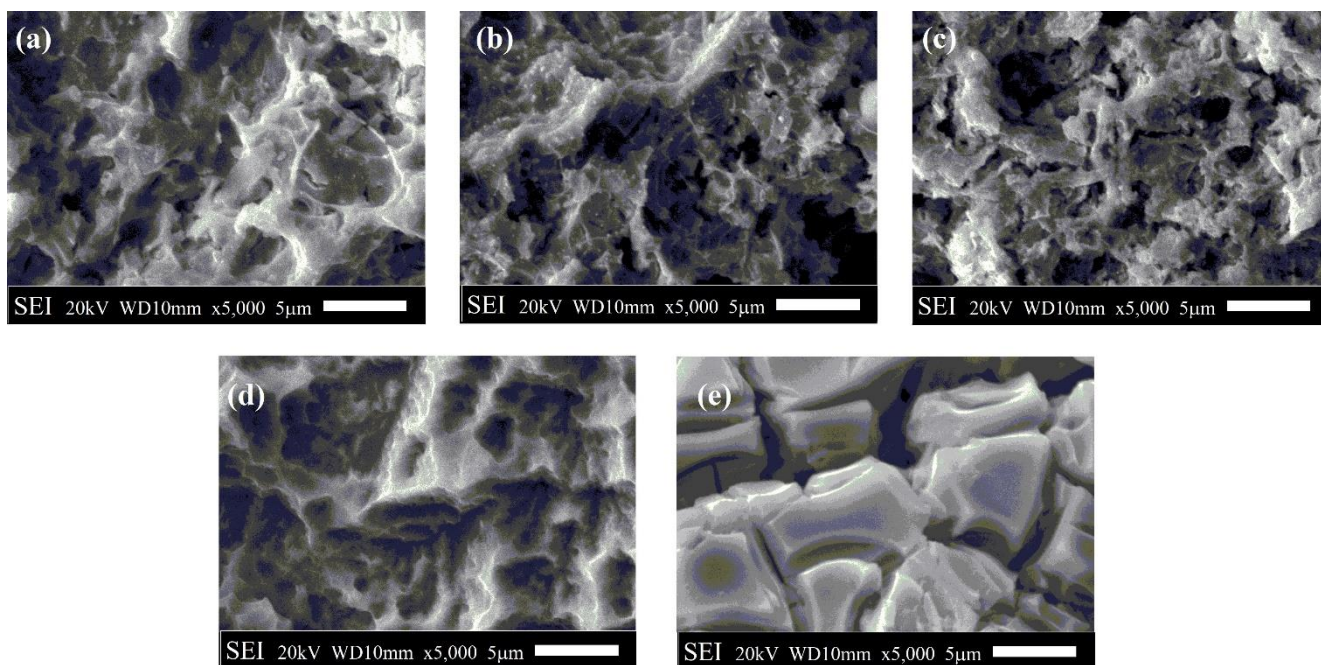


**Figure 2.** SEM images obtained at 5000X–SEI for the DSAs: a) DSA–1, b) DSA–2, c) DSA–3, d) chemically pretreated Ti, and e) commercial DSA of  $\text{Ti}|\text{IrO}_2\text{--SnO}_2\text{--Sb}_2\text{O}_5$ .

If the Sn content in the oxide film increases, the cracked morphology disappears, and a more agglomerated surface is observed [27, 28]. In this work, the Sn concentration (89 mM) used in all the precursor solutions yielded DSA surfaces with shallow cracking features. The lack of cracking and adequate roughness of oxide films are essential factors to consider since the durability, mechanical stability, and corrosion resistance of DSA type electrodes are generally influenced by their morphology [29].

To determine the crystal structure of the metal oxide films formed on the DSA surfaces, XRD analysis was performed.

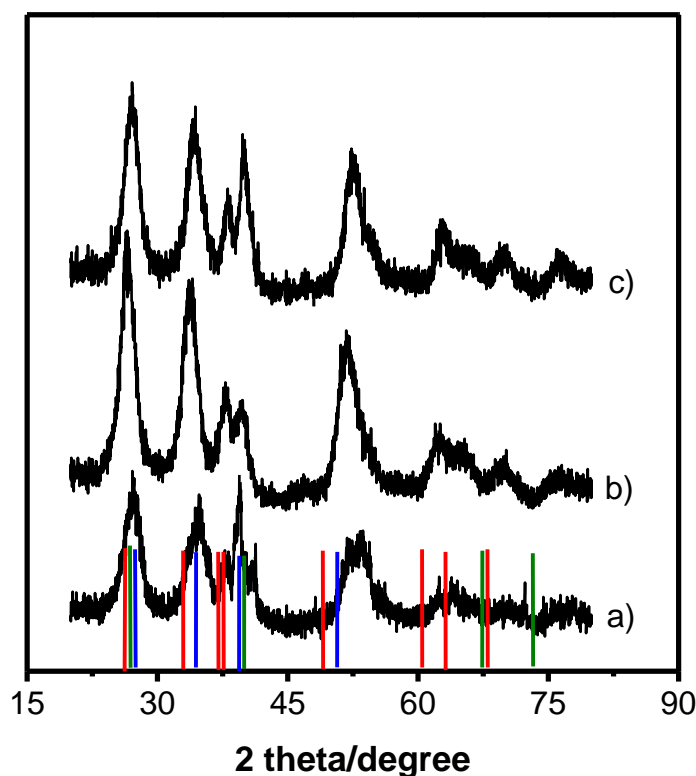


**Figure 3.** Diffraction patterns of the different DSAs: a) DSA-1, b) DSA-2, and c) DSA-3. The colored lines correspond to the database diffraction patterns for SnO<sub>2</sub> (blue), IrO<sub>2</sub> (red), and Sb<sub>2</sub>O<sub>3</sub> (green).

Figure 3 shows the diffractograms obtained for each DSA electrode; these were compared with patterns from the International Centre for Diffraction Data (ICDD) database, PDF files 04-003-0649 for SnO<sub>2</sub>, 04-009-8479 for IrO<sub>2</sub>, and 00-043-1071 for Sb<sub>2</sub>O<sub>3</sub>. The low intensities of the peaks obtained for all the DSA surfaces were due to the thin coating and low crystallinity.

It was observed that the crystalline phases of the different metal oxides vary with their composition in the coating. Note that the sample corresponding to DSA-2 revealed higher relative intensities and smaller widths of the observed peaks. A similar trend is observed for DSA-3 but with lower values. This behavior is interesting because DSA-3 had a higher content of Ir in its polymeric solution but exhibited slightly less crystallinity than DSA-2. On the other hand, DSA-1 showed the most amorphous structure.

For this reason, it was essential to evaluate the elemental distribution on the electrode surface. Figure 4 shows the distribution of each metal detected by EDX microanalysis for the different electrodes. The order of the Ir distribution is as follows: DSA-3 > DSA-2 > DSA-1. This behavior is concordant with the concentrations used in the polymeric precursor solution since the solution used for the preparation of DSA-3 contained more Ir than that used for the preparation of DSA-2 and DSA-1. Regarding the Sn distribution, DSA-1 (Figure 4-a) had a better distribution than the other DSAs, even though DSA-2 had twice the concentration of this precursor.

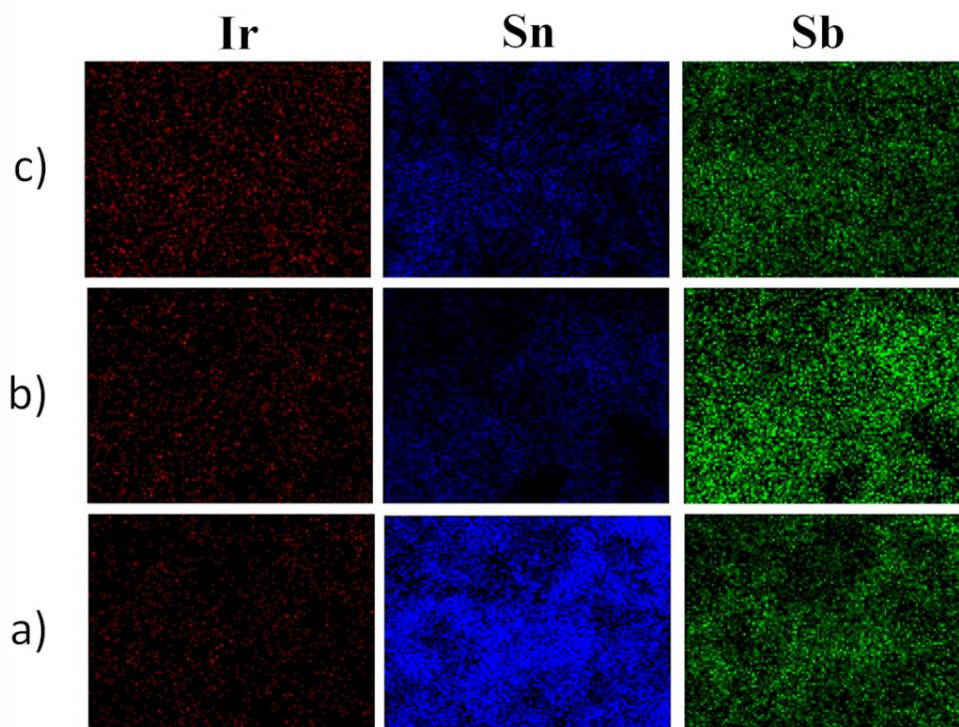


**Figure 4.** EDX mapping at 1000X for DSAs (a) DSA–1, (b) DSA–2, and (c) DSA–3, where Ir, Sn, and Sb are represented in red, blue, and green, respectively.

Finally, although the Sb concentration remained constant in each polymeric precursor, a better distribution was observed in DSA–2 than in DSA–1 and DSA–3. In this way, the weight percentage obtained by DRX was compared to that calculated by EDX with INCA software.

An analysis of the values shown in Table 1 allows us to determine that tin oxide is present in a major proportion in all DSAs prepared in this work (>70% weight). However, according to the mapping images observed in Figure 4, the oxide amounts on the DSA surface do not agree with the molar composition of the precursor in the polymeric solution.

**Table 1.** Weight percentage of each oxide that was calculated by DIFFRAC.EVA software for XRD and INCA software for EDX

	Oxide content (%)					
	Sn		Sb		Ir	
	XRD	EDX	XRD	EDX	XRD	EDX
DSA–1	86.7	89.52	2.4	1.47	10.9	9.01
DSA–2	85.4	86.69	1.0	0.15	13.6	13.16
DSA–3	74.9	75.37	0.9	0.64	24.2	24.00

### 3.1.1 Reactions involved in the production of metal oxides

According to the XRD studies, SnO<sub>2</sub>, IrO<sub>2</sub>, and Sb<sub>2</sub>O<sub>3</sub> were formed during the calcination process. To understand how these oxides are created, it was necessary to consider the Kolbe reaction basis, which has been previously reviewed for some systems [30].

The Kolbe reaction is a thermodynamically favorable process that involves the oxidation of a carboxylate and release of CO<sub>2</sub> as a highly stable molecule and organic free radicals that dimerize effortlessly. Such a dissociative response also promotes free radical formation from other organic anions [31]. In this regard, metallic precursor anions can be viewed as good reducing agents, whereas metallic cations represent suitable oxidizing species. Under the conditions of high calcination temperature, the proposed precursor combination promotes redox reactions that yield metallic oxides [32]. Considering these thermally activated redox reactions, the metallic cations are reduced to the metal state and then become metal oxides by reactions with the diatomic oxygen present in the calcination medium at high temperature. On the other hand, organic anions are oxidized to volatile organic molecules. At high temperatures, these molecules can be oxidized by electron transfer and further transformed into free radicals, CO<sub>2</sub>, and H<sub>2</sub>O through decarboxylation and/or combustion processes, which is an advantage because the polymeric coatings would not contain undesirable residues. Table 2 shows a proposal for the reactions that could be involved in the transformation of Sn(II) acetate, Ir(III) acetylacetonate, and Sb(III) acetate to their respective oxides: SnO<sub>2</sub>, IrO<sub>2</sub>, and Sb<sub>2</sub>O<sub>3</sub> (Equations 2, 5, and 10).

**Table 2.** Reactions proposed to obtain Sb<sub>2</sub>O<sub>3</sub>, SnO<sub>2</sub>, and IrO<sub>2</sub> from iridium(III) acetylacetonate, tin(II) acetate, and antimony(III) acetate used as metallic precursors.

Oxide	Chemical reactions	Equations
<b>Sb<sub>2</sub>O<sub>3</sub></b>	$Sb(CH_3COO^-)_{3(s)} \xrightarrow{\Delta} Sb_{(s)}^0 + 3CO_{2(g)} + 3CH_3^{\bullet}(g) \rightarrow Sb_{(s)}^0 + 3CO_{2(g)} + 3/2(CH_3-CH_3)_{(g)}$	(1)
	$4Sb_{(s)}^0 + 3O_{2(g)} \xrightarrow{\Delta} 2Sb_2O_{3(s)}$	(2)
	$(CH_3-CH_3)_{(g)} + 7/2 O_{2(g)} \rightarrow 2CO_{2(g)} + 3H_2O_{(g)}$	(3)
<b>SnO<sub>2</sub></b>	$Sn(CH_3COO^-)_{2(s)} \xrightarrow{\Delta} Sn_{(s)}^0 + 2CO_{2(g)} + 2CH_3^{\bullet}(g) \rightarrow Sn_{(s)}^0 + 2CO_{2(g)} + (CH_3-CH_3)_{(g)}$	(4)
	$Sn_{(s)}^0 + O_{2(g)} \xrightarrow{\Delta} SnO_{2(s)}$	(5)
	$(CH_3-CH_3)_{(g)} + 7/2 O_{2(g)} \rightarrow 2CO_{2(g)} + 3H_2O_{(g)}$	(6)
<b>IrO<sub>2</sub></b>	$[CH_3(C=O)CH=C(O^-)CH_3]_3Ir_{(s)} \xrightarrow{\Delta} Ir_{(s)}^0 + 3[CH_3COCH=C(O^{\bullet})CH_3]_{(g)}$	(7)
	$3[CH_3COCH=C(O^{\bullet})CH_3]_{(g)} \rightarrow 3[CH_3(C=O)(C^{\bullet}H)(C=O)CH_3]_{(g)}$	(8)
	$3[CH_3(C=O)(C^{\bullet}H)(C=O)CH_3]_{(g)} \rightarrow 3/2 [CH_3(C=O)(CH)(C=O)CH_3]_{2(s)}$	(9)
	$Ir_{(s)}^0 + O_{2(g)} \xrightarrow{\Delta} IrO_{2(s)}$	(10)
	$2[CH_3(C=O)(CH)(C=O)CH_3]_{2(s)} + 23O_{2(g)} \xrightarrow{\Delta} 20CO_{2(g)} + 14 H_2O_{(g)}$	(11)

Note that these global reactions were proposed under the consideration that metal oxides are formed, as well as the fact that the decarboxylation and combustion of organic species have been widely documented in the literature [30, 31–33].

The activation step is thermal and involves the oxidation of either acetate or acetylacetonate. In contrast, their driving force is determined by the high stability of the products involved in the decarboxylation, dimerization, and combustion reactions.

### 3.2 Electrochemical characterization

Cyclic voltammetry was used to evaluate the electrocatalytic properties of each synthesized electrode. Figure 5–a shows the voltammetric behavior in 1 M HClO<sub>4</sub>. All electrodes show a redox signal in the potential region between 0.2 and 1.0 V/SCE. This electrochemical process is attributed to the Ir<sup>3+</sup>/Ir<sup>4+</sup> redox pair from IrO<sub>2</sub>, which is in agreement with previous reports [29, 34].

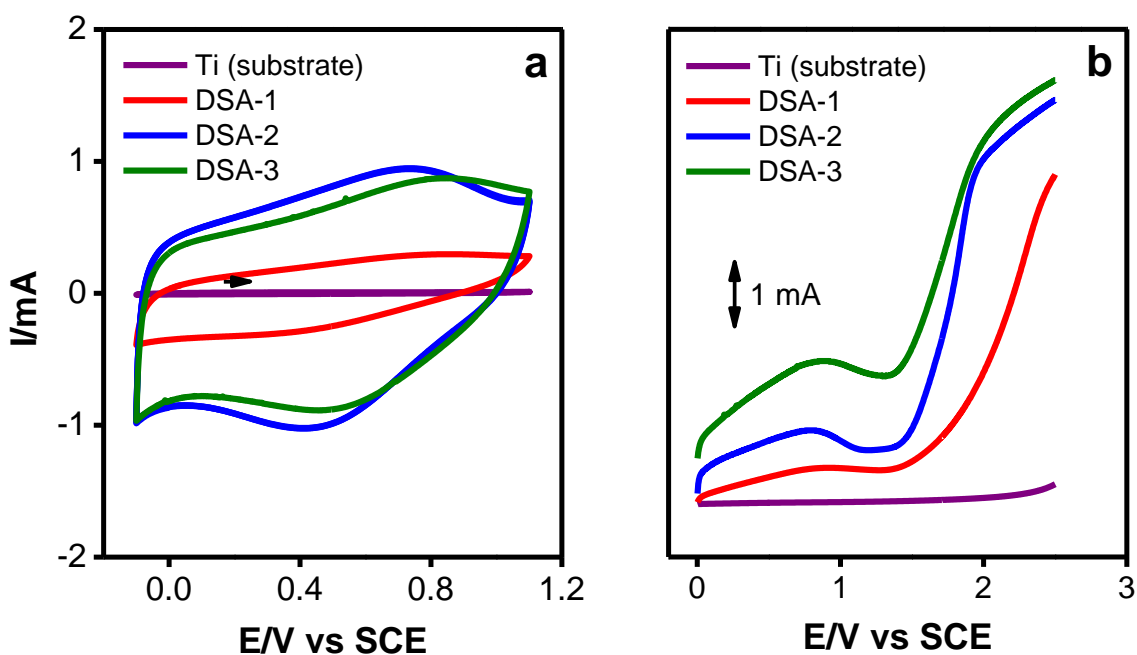


**Figure 5.** (a) Cyclic voltammograms and (b) linear sweep voltammograms obtained for the Ti substrate (purple curve) and DSAs in 1 M HClO<sub>4</sub> at 0.1 V s<sup>-1</sup>.

Although the Ir precursor concentration was the same for DSA-1 and DSA-2, a higher current was observed for the latter, possibly due to a different distribution on the electrode surface. DSA-2 and DSA-3 had the highest current, which is in agreement with the distribution of Ir observed by EDX mapping (Figure 4).

On the other hand, Figure 5–b presents the linear sweep voltammetry curves obtained over a wide potential range for the uncoated Ti substrate and DSAs. The purpose of these experiments was to evaluate the oxygen evolution overpotential of each electrode. This reaction competes with the formation

of hydroxyl radicals ( $\bullet\text{OH}$ )<sub>ads</sub>, which is the desired intermediate on both *active* and *non-active* surface electrodes.

For the case of the pure Ti substrate, no significant current is observed during the entire range of potentials surveyed. In contrast, a significant current increase was observed near 1.3 V/SCE for all DSAs. This phenomenon is due to the oxidation of water producing oxygen, which is catalyzed by the presence of IrO<sub>2</sub> [9, 35]. It is noteworthy that none of the DSAs synthesized in this work corroded during these polarization measurements, which indicates their high anodic stability.

### 3.2.1 Production of hydroxyl radicals

It is known that hydroxyl radicals react with coumarin to generate 7-hydroxycoumarin [36], as schematized in inset-a of Figure 6. Thus, this reaction serves as an indirect test of hydroxyl radical production. Figure 6 shows absorbance measurements carried out after the electrolysis of coumarin in a 0.1 M Na<sub>2</sub>SO<sub>4</sub> solution. The absorbance band ( $\lambda_{\text{max}} = 277 \text{ nm}$ ) of the initial coumarin ( $C_0$ ) decreases after 20 min of electrolysis; the extent of the decrease is in the order DSA-1 > DSA-2 > DSA-3. This tendency is consistent with the increase in fluorescence intensity related to the formation of 7-hydroxycoumarin (inset-b). In this way, the results confirm the generation of  $\bullet\text{OH}$  radicals by all DSAs.

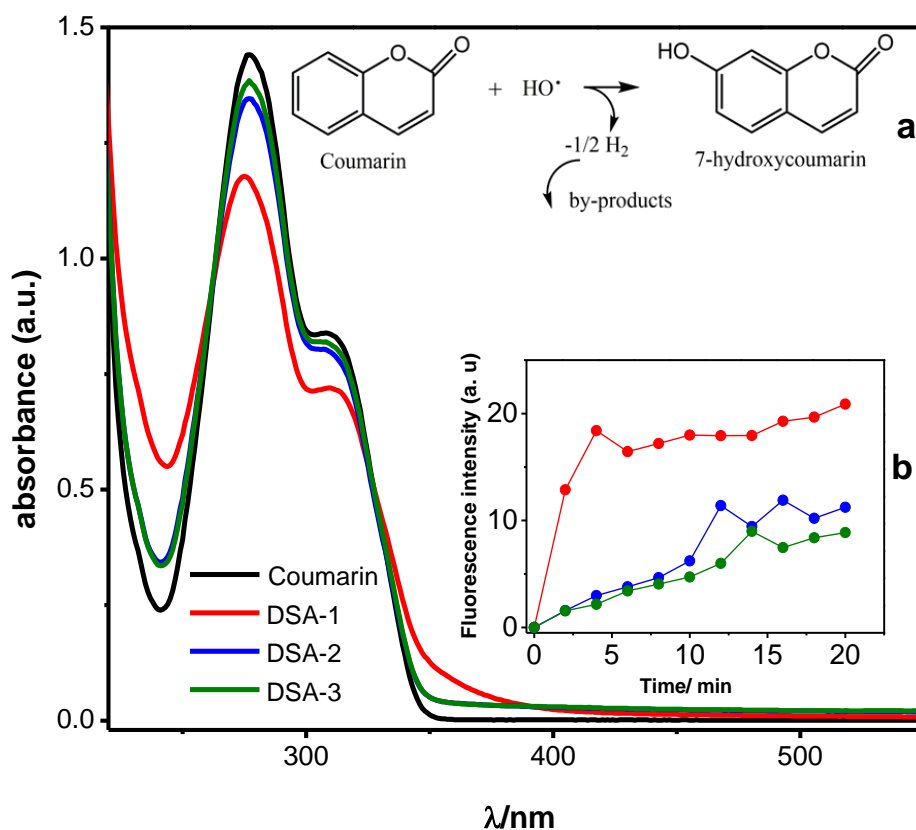


**Figure 6.** UV-Vis spectra of 0.1 mM coumarin + 0.1 M Na<sub>2</sub>SO<sub>4</sub> in water before and after 20 min of electrolysis by imposing  $8 \text{ mA cm}^{-2}$  on DSAs. **Insets:** (a) coumarin reaction with hydroxyl radicals (released hydrogen can react further to yield other byproducts) and (b) variation of the 7-hydroxycoumarin fluorescence intensity with electrolysis time for each DSA electrode.

A high surface roughness is required to obtain low electrolysis times during pollutant degradation. For this reason, the real area of each DSA electrode was determined, as explained in section 2.2.2. The roughness factor, defined as the real surface area per apparent geometric area, was evaluated according to the procedure reported [37]. The obtained values were  $24.9 \pm 0.8$ ,  $67.1 \pm 1.3$ , and  $77.6 \pm 1.8$  for DSA-1, DSA-2, and DSA-3, respectively.

The roughness factor was on the same order of magnitude for all DSAs, but DSA-1 presented the lowest value. This behavior is consistent with that observed in Figure 5-a. Evaluation of the overall behavior of DSAs is, in fact, a complicated process. However, a significant contribution was obtained from the ternary mixture, which is an interesting approach for pollutant treatment applications.

### 3.3 Oxidation of organic pollutants

Electrochemical processes are versatile since they may be applied to direct and indirect oxidation reactions for pollutant degradation. Direct oxidation occurs on the electrode surface (direct electron transfer), while indirect oxidation generates strong oxidants that subsequently react with the organic material [38].

In this sense, the activity of DSAs was tested to oxidize two organic pollutants: tartrazine (a hydrosoluble dye) and dibenzothiophene (a liposoluble sulfur compound). These experiments aimed to demonstrate the environmental use of the synthesized DSAs in water and organic media. Total electrolysis experiments were conducted under different conditions, depending on the pollutant to be treated.

#### 3.3.1 Tartrazine (TRZ)

Cyclic voltammetry was performed on a glassy carbon electrode to evaluate the degradation of tartrazine after electrolysis. As shown in Figure 7-a, tartrazine oxidation (peak I) occurs at 0.94 V/SCE (black curve). This peak disappears after electrolysis on the DSA-1 electrode, indicating the full conversion of TRZ. The same result was obtained on DSA-2 and DSA-3 (data not shown). Additionally, tartrazine decolorization was analyzed by UV-vis spectrophotometry at several time intervals (Figure 7-b).

The principal absorbance band ( $\lambda_{\text{max}} = 430 \text{ nm}$ ) corresponds to the  $-\text{N}=\text{N}-$  group that confers a yellow color to the TRZ molecule [39]. It is possible to visualize that more than 95% of the initial tartrazine band at  $\lambda_{\text{max}}$  decreased using the DSA-1 electrode. The results obtained with DSA-2 and DSA-3 are not shown because they were very similar. Thus, the decrease in this band implies a decolorization process.

The degradation of tartrazine ( $50 \text{ mg L}^{-1}$ ) using three methods was reported by Santos [40]. When they applied  $50 \text{ mA cm}^{-2}$  for 120 min on a  $\text{TiO}_2\text{-RuO}_2$  electrode, 88% decolorization was obtained. On the other hand, Zhang [41] obtained 90% decolorization of tartrazine ( $40\text{--}100 \text{ mg L}^{-1}$ ) by using an electro-Fenton process on a  $\text{Ti|IrO}_2\text{-RuO}_2$  anode and applying a  $25 \text{ mA cm}^{-2}$  current density for 30 min. Our results (95% decolorization of  $40 \text{ mg L}^{-1}$  TRZ) are comparable to those mentioned above but used a

current density that was from  $\sim 3$  to  $\sim 6$  times lower, with the advantage of dispensing chloride ions for the preparation of the electrodes.

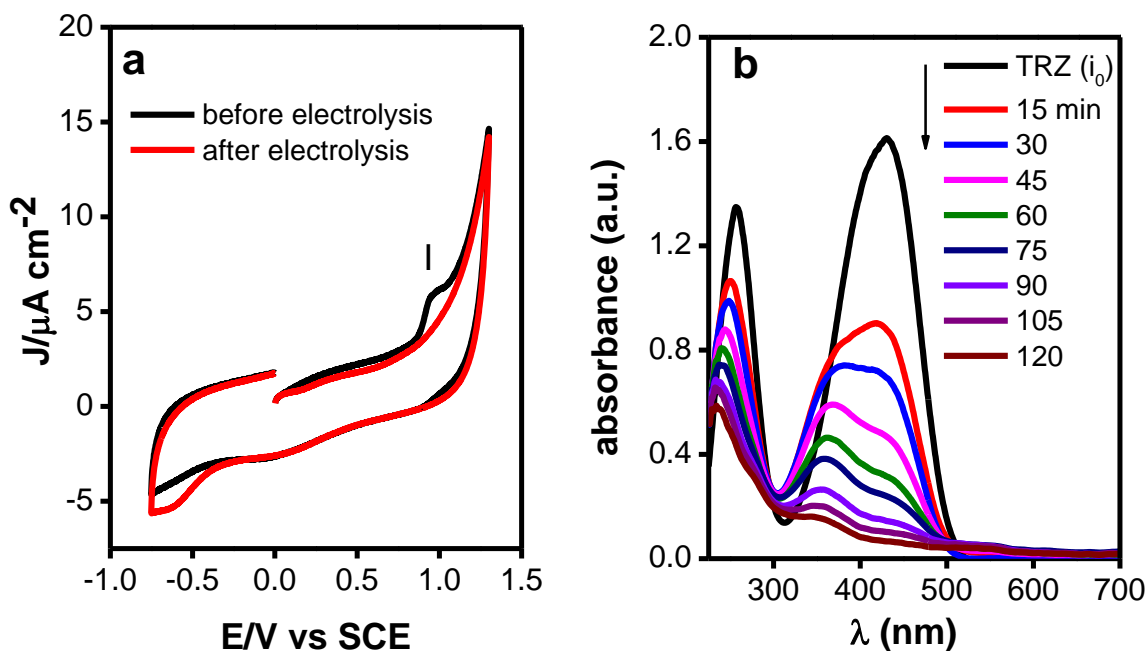


**Figure 7.** (a) Cyclic voltammetry (scan rate:  $0.1 \text{ V s}^{-1}$ ) performed on glassy carbon electrodes (3 mm diameter) before (black curve) and after (red curve) electrolysis; and (b) UV-Vis spectra at different electrolysis times (on a DSA-1 electrode by applying a  $8 \text{ mA cm}^{-2}$  current density) for 40 ppm tartrazine dissolved in  $\text{H}_2\text{O} + 0.1 \text{ M Na}_2\text{SO}_4$ .

The absorbance band at 250 nm corresponds to the aromatic ring of the dye. This band also decreases but at a slow rate due to the difficulty of rupturing the aromatic structure. After 120 min of electrolysis, this band is not eliminated, which implies that the molecule is not completely mineralized. For this reason, TOC measurements were performed after treatment to determine the ability of the synthesized electrode to mineralize tartrazine. Mineralization values of 66%, 71%, and 67% were obtained with DSA-1, DSA-2, and DSA-3, respectively.

To investigate the products generated due to the electrolysis process, samples of the treated solutions were subjected to HPLC-MS-TOF analysis. The main peak was obtained at 2.5 min. The ESI analysis showed a molecular ion at  $m/z = 226.94$  ( $[\text{M}-\text{H}]^+$ ), which corresponds to **7** in Figure 8. The proposed compound attributed to this fragment ion was identified as an amino sulfonate fragment. Figure 8 shows a proposal for the possible mechanism of the mediated oxidation of TRZ (**1**).

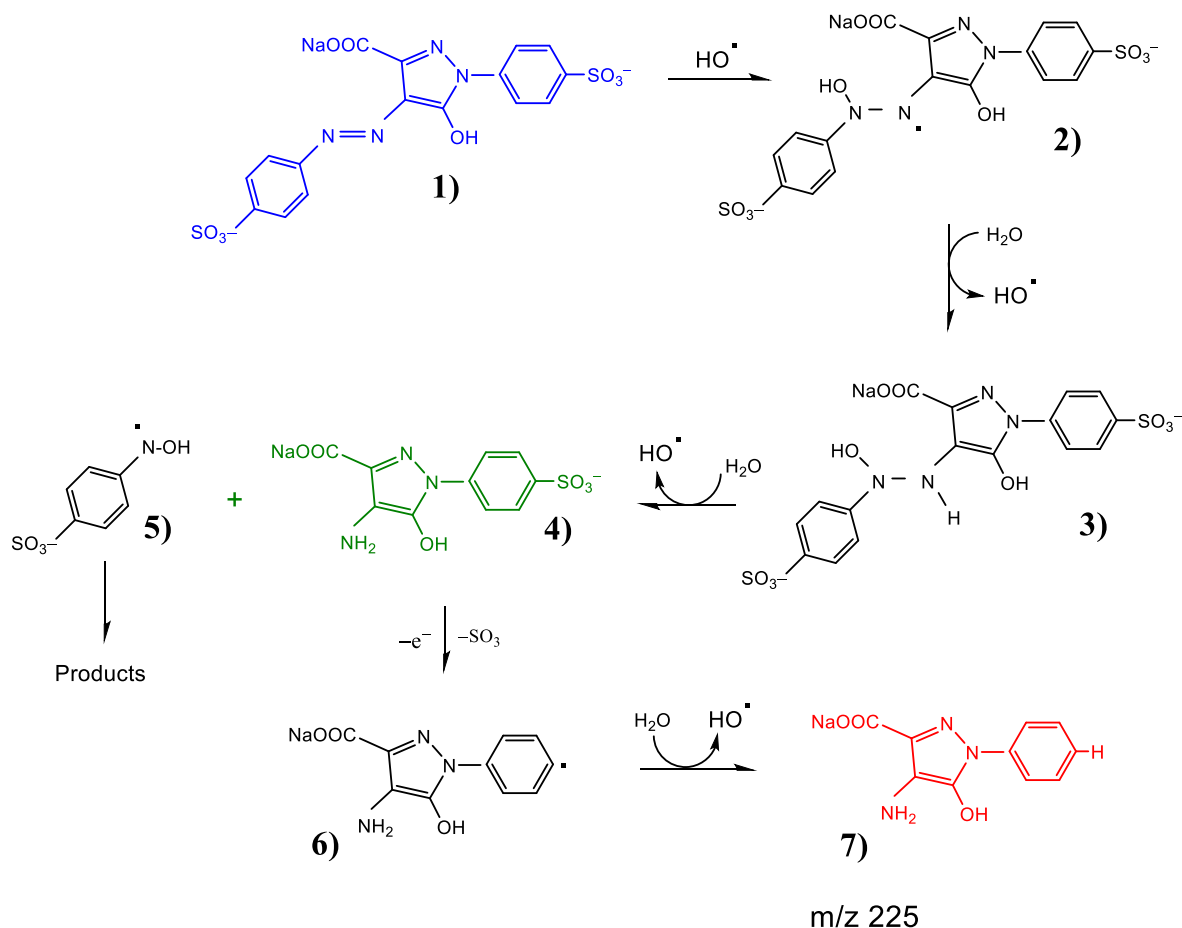


**Figure 8.** Proposed reaction mechanism for the decomposition of 40 ppm tartrazine in  $\text{H}_2\text{O} + 0.1 \text{ M Na}_2\text{SO}_4$  using the synthesized DSAs and applying a  $8 \text{ mA cm}^{-2}$  current density for 120 min.

The degradation mechanism starts with water oxidation to form  $\bullet\text{OH}$  radicals that attack the double bond of the azo group ( $-\text{N}=\text{N}-$ ) of TRZ [40], which is in agreement with the discoloration of the dye, as shown in Figure 7-b. This allows OH addition to the left nitrogen and leaves an unpaired electron on the right nitrogen (2). Due to the high reactivity of this site, it reacts with water and breaks it homolytically. This reaction yields 3, whose hydrolysis releases 4, and free radical 5 that decomposes into nondetected products. Since electrolysis was carried out at an oxidizing potential, the sulfonate group  $-(\text{SO}_3^-)$  in 4 would be oxidized together with the release of  $\text{SO}_3$ . This reaction releases free radical 6, whose reaction with water yields final product 7. These reactions with water always yield a hydroxyl radical, which is used in further decomposition reactions of TRZ.

### 3.3.2 Dibenzothiophene (DBT)

Figure 9 shows the voltammetric behavior of DBT on a glassy carbon electrode before and after electrolysis on DSA-1. It initially presents three oxidation peaks, and according to our previous results, peak I is attributed to the oxidation of dibenzothiophene, while peaks II and III correspond to the oxidation of dibenzothiophene sulfoxide and dibenzothiophene sulfone, respectively [24].

As shown in Figure 9, the intensities of the three peaks decrease after electrochemical treatment, and peak I almost disappears after 90 minutes of electrolysis (~80% DBT conversion). This result was similar for DSA-2 and DSA-3 electrodes and suggests the possibility of converting dibenzothiophene to dibenzothiophene sulfoxide and its respective sulfone through direct oxidation on DSAs in acetonitrile/water media [24].

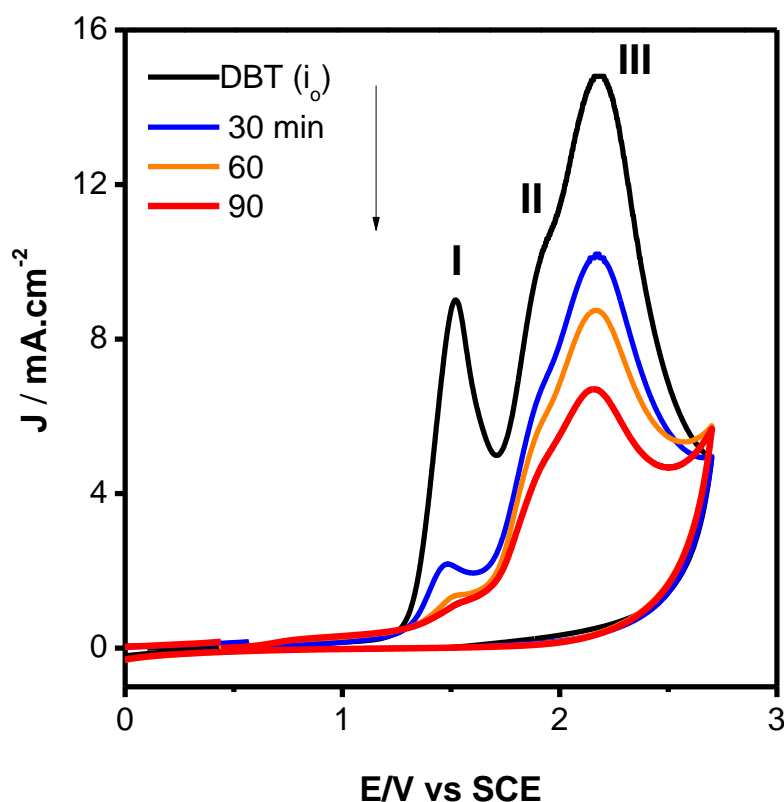


**Figure 9.** Cyclic voltammetry of 200 ppm dibenzothiophene in  $\text{CH}_3\text{CN} + 1.6 \text{ M H}_2\text{O} + 0.1 \text{ M Et}_4\text{NNBF}_4$  at  $0.1 \text{ V s}^{-1}$  on a glassy carbon electrode (3 mm diameter) under a  $\text{N}_2$  atmosphere before (black curve) and after different times of electrolysis (colored curves) using a DSA-1 electrode.

Note that TOC cannot be measured for the DBT-treated samples due to the volatile organic solvent in which it was dissolved.

To date, there are no reports about the oxidation of DBT on DSAs. For diesel-type fuel, Abdullah and Xing reported the oxidation of DBT by generating  $\text{H}_2\text{O}_2$  on a cathode made of carbon black/polytetrafluoroethylene particles [42]. Their process took 6 h to attain a 97.8% conversion of 500 ppm DBT.

Note that in this work, the oxide films formed on all DSAs showed excellent mechanical resistance during TRZ and DBT electrolysis.

### 3.3.3 Efficiency and energy consumption

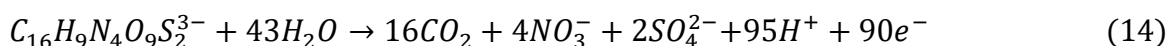
The electrolysis performance of the process for the degradation of TRZ and DBT was evaluated from a quantitative perspective. Parameters such as efficiency and energy consumption during electrolysis are essential to characterize electrochemical processes focused on removing organic pollutants.

For TRZ, Equations 12 and 13 [43] were used to determine the energy consumption factor and current efficiency, respectively, based on TOC measurements.

$$\phi(\%) = \frac{(\Delta TOC)_{exp} n F V_{sol}}{4.32 \times 10^7 m I t} \times 100 \quad (12)$$

$$E_c = \frac{E_{cell} I t}{V_{sol}} \quad (13)$$

$\phi(\%)$  is the mineralization current efficiency,  $n$  is the total number of electrons consumed ( $n = 58$  for tartrazine according to Equation 14 [44]),  $(\Delta TOC)_{exp}$  is the experimental TOC decay (mg carbon L<sup>-1</sup>),  $F$  is the Faraday constant (96485 C mol<sup>-1</sup>),  $V_{sol}$  is the solution volume (L),  $m$  is the number of pollutant carbon atoms (16 carbon atoms for TRZ),  $4.32 \times 10^7$  is a conversion factor ( $3600 \text{ s h}^{-1} \times 12000 \text{ mg carbon mol}^{-1}$ ),  $t$  is the electrolysis time (h),  $E_c$  is the energy consumption (kWh m<sup>-3</sup>),  $I$  is the applied current (A), and  $E_{cell}$  is the average cell potential (V).



On the other hand, to evaluate the current efficiency and energy consumption in the oxidation of DBT, Equations 15 and 16 were used [45].

$$\phi(\%) = \frac{4 F V [COD_0 - COD_f]}{I t} \times 100 \quad (15)$$

$$E_c = \frac{4 F E_{cell}}{\phi V_m} \frac{1}{3.6} \quad (16)$$

where  $\phi(\%)$  is the current efficiency,  $V_m$  is the molar solution volume (cm<sup>3</sup> mol<sup>-1</sup>),  $t$  is the time of electrolysis (s), and  $E_c$  is the energy consumption (kWh m<sup>-3</sup>).  $COD_0$  and  $COD_f$  represent the initial and final chemical oxygen demand (COD), respectively; however, in this work, these values were changed by the pollutant concentrations (mol cm<sup>-3</sup>) because COD measurements are not possible in organic media. The value of 3.6 is a correction factor that converts  $E_c$  to units of kWh m<sup>-3</sup>. In this sense, the conversion percentages to dibenzothiophene sulfones were 81.2%, 85.5%, and 89.9% for DSA-1, DSA-2, and DSA-3, respectively.

The current efficiency and energy consumption for both TRZ and DBT are shown in Table 3. All DSAs showed similar current efficiencies and energy consumption values for each pollutant evaluated. These values were smaller than those reported by other authors, where maximum current efficiency values (37–45%) were reached in 60–120 min of treatment [46, 47]. The small values of

current efficiency obtained here can be attributed to many factors, such as low  $\bullet\text{OH}$  production, the generation of byproducts that are hard to oxidize [43, 46–48]. In addition, the use of higher current densities can promote parasitic reactions such as the production of other oxidizing agents ( $\text{H}_2\text{O}_2$ ,  $\text{SO}_4\bullet^-$ , and  $\text{S}_2\text{O}_8^{2-}$ ), with the release of hydroxyl radicals in a lesser extent [49].

**Table 3.** Current efficiency and energy consumption for the degradation of tartrazine and dibenzothiophene on DSAs.

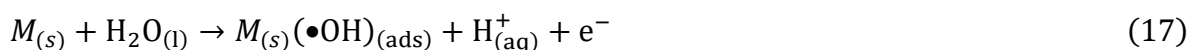
Electrodes	Tartrazine		Dibenzothiophene	
	$\emptyset(\%)$	$\text{Ec}/\text{kWh m}^{-3}$	$\emptyset(\%)$	$\text{Ec}/\text{kWh m}^{-3}$
DSA-1	$7.74 \pm 0.2$	$42.24 \pm 2.7$	$5.46 \pm 0.2$	$95.61 \pm 4.4$
DSA-2	$8.33 \pm 0.3$	$36.48 \pm 4.0$	$5.75 \pm 0.3$	$90.80 \pm 3.9$
DSA-3	$7.78 \pm 0.5$	$38.40 \pm 2.1$	$6.05 \pm 0.2$	$86.36 \pm 2.0$

Additionally, it is important to emphasize that these experiments were carried out in a divided cell, and consequently, only the anode contributed to the degradation of the pollutant. The electrolysis experiments were performed under conditions where competence with water oxidation can occur, which would be a factor leading to a decrease in the current efficiency of the process.

### 3.4 Proposal of “subnon–active” anode surfaces

According to Comninellis [1], partial oxidation of organic compounds in an aqueous solution is shown by anodes with low oxygen evolution overpotentials; they are promising electrocatalysts for the oxygen evolution reaction. Therefore, they have been called “*active*.” This behavior is shown by electrodes made of transition metal oxides ( $\text{IrO}_2$  and  $\text{RuO}_2$ ), Pt, carbon, and graphite electrodes. On the other hand, anodes with a high oxygen evolution overpotential, such as boron-doped diamond electrodes (BDDs), are called “*non–active*,” which means they are poor electrocatalysts for the oxygen evolution reaction. This characteristic allows the complete mineralization of organic compounds during an oxidation process.

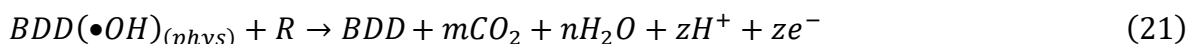
Steps for oxidizing organic pollutants in an aqueous solution using *active* or *non–active* anodes have been proposed since the 1990s [1]. The initial step occurs on the electrode surface sites  $M_{(s)}$ , which involves the one-electron oxidation of water to yield adsorbed hydroxyl radicals (Equation 17). In this activation process, the inner sphere character of electron transfer activation is determined by the electrocatalytic interaction of water with the electrode surface.



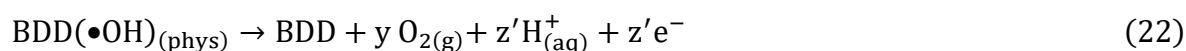
Depending on the chemical reactivity of the metallic sites that contain  $M_{(s)}$ , water oxidation on metallic oxide sites ( $MO_x$ ) can also be carried out. Thus, on *active* electrodes, the surface ( $MO_x$ ) allows the formation of a chemisorbed “active oxygen” adduct, commonly called a superoxide or higher oxide,  $MO_x(\bullet OH)_{(chs)}$  (Equation 18), whose oxidation releases a proton and yields reactive oxide  $MO_{x+1}$ . This new species can decompose organic compounds ( $R$ ) through oxygen transfer reactions (Equation 19). Consequently, this process also allows the recovery of the original  $MO_x$  sites that induce further water oxidation. Due to the high reactivity of the  $MO_{x+1}$  transient oxide sites, they can also be decomposed into molecular oxygen and  $MO_x$  (Equation 20). This competitive reaction represents a drawback because part of the total charge transferred during the overall electrolysis process is lost in a nonuseful reaction, so very long electrolysis times are needed during the experiment.



In contrast, in the case of *non-active* surfaces such as those of BDD electrodes, the reactive oxygen species are weakly adsorbed (physisorbed) on the surface,  $BDD(\bullet OH)_{phys}$  (Equation 21). The weak nature of the interaction between the hydroxyl radical and the BDD surface allows for the complete incineration of organic compounds (nonselective oxidation). In this sort of electrode, the degradation reaction is mediated by hydroxyl radicals ( $\bullet OH$ ), which are stabilized on the electrode surface [50].



In any case of *active or non-active* anodes, chemisorbed or physisorbed hydroxyl radicals are involved during the partial conversion or complete mineralization (combustion) of organic compound  $R$ , respectively (Equations 19 and 21). In both cases, dioxygen evolution (Equations 20 and 22) is a competitive reaction that diminishes the degradation efficiency.



The  $MO_{x+1}/MO_x$  pair behaves as a mediator for oxygen production because it decomposes to  $O_2$  and  $MO_x$ , allowing the original oxide sites to recover. However, on BDD surfaces, Equation 21 competes with the direct side oxidation to  $O_2$ , even though the oxygen evolution reaction (Equation 22) occurs in a lower proportion. For this reason, partial or complete mineralization of organic pollutants is strongly dependent on the nature of the electrode surface ( $M_s$  and/or  $MO_x$ ) [50].

Some DSA type electrodes synthesized with lead dioxide or tin dioxide or those formed by oxide combinations such as antimony-doped tin oxide are classified as *non-active* anodes; however, the mineralization percentage of organic compounds obtained from industrial wastewater using  $PbO_2$  and  $SnO_2$  is not as high as that obtained with BDD electrodes [4]. Mineralization percentages obtained in less than 2 hours of electrolysis on BDD electrodes are almost 100%. However, pollutant mineralization using  $PbO_2$  and  $SnO_2$  electrodes is lower than that using BDD (~70%). These results mean that  $PbO_2$

and SnO<sub>2</sub> can oxidize organic pollutants by generating hydroxyl radicals in the same way as BDD but with a lower mineralization efficiency. Other authors have improved the lifetime and stability of Sn–Sb electrodes by doping them with Ir and Ru, as is carried out for the degradation of nitrophenols [51]. The best results were obtained using the Ti|SnO<sub>2</sub>–Sb<sub>2</sub>O<sub>5</sub>–IrO<sub>2</sub> electrode.

In this context, it is essential to classify lead dioxide and tin dioxide anodes, DSA type electrodes formed by oxide combinations such as antimony-doped tin oxide as well as the electrodes synthesized in this work in a new category considering •OH generation. We suggest the term “*subnon-active*”, where almost complete mineralization can be obtained. The process involved in this kind of electrode suggests the possibility that the hydroxyl radicals are in equilibrium between the chemisorbed and physisorbed states (Equation 23). This means that the chemisorbed species yield the partial decomposition of R, while the physisorbed species allow for a mineralization degree. From a chemical point of view, the competition between both processes depends on the affinity of the hydroxyl radicals for the free metal and/or metallic oxide sites on the electrode surface. From a practical point of view, the predominance of the mineralization process also depends on competition between the electrolysis rate and the rate of the forward and backward reactions involved in the chemisorption-physisorption equilibrium (Equation 23).

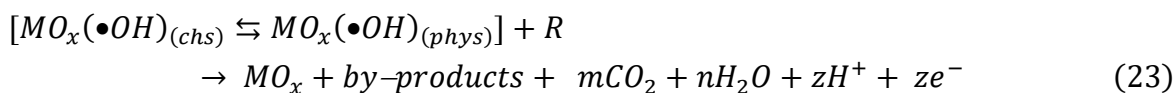
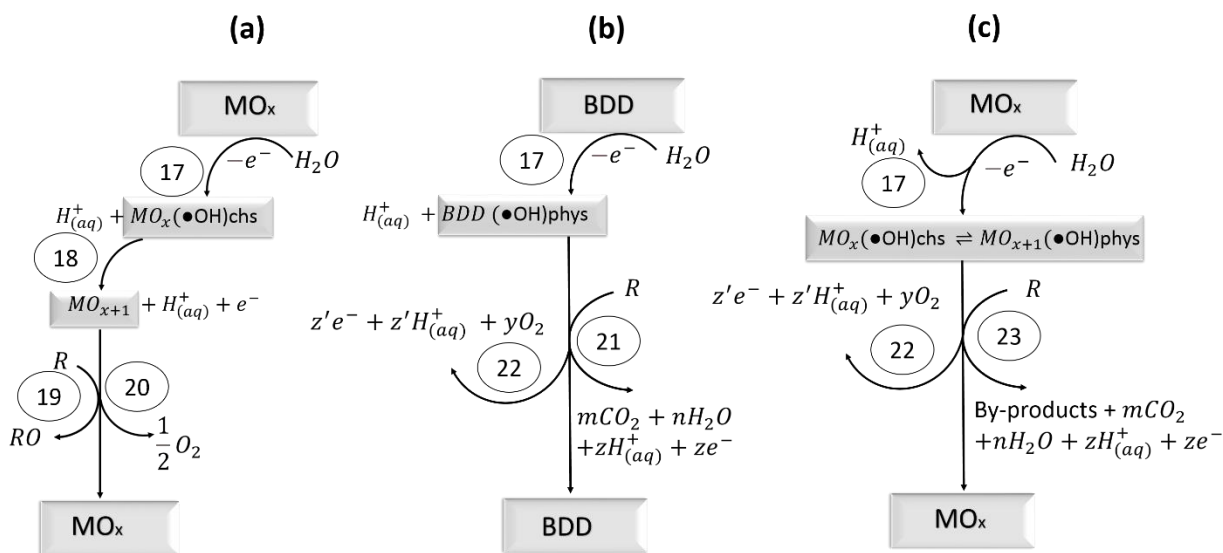


Figure 10 shows a proposal representing the different anode surfaces as *active*, *non-active* (BDD electrodes), and *subnon-active*, a new classification recommended in this work.



**Figure 10.** Anodic oxidation scheme for (a) *active*, (b) *non-active*, and (c) *subnon-active* (proposed in this work) electrode surfaces.

Because chemisorption changes the electronic properties of the species on the surface, the detection of  $\bullet\text{OH}$  radicals on active anodes such as Pt and  $\text{IrO}_2$  is negligible. However, on  $\text{SnO}_2$  anodes, the accumulation of  $\bullet\text{OH}$  radicals has been possible [1]. Therefore, *subnon-active* anodes have the possibility of stabilizing hydroxyl radicals that can interact with organic compounds; however, the degradation of the organic compounds does not reach complete incineration.

Due to its higher proportion of oxide surface  $\text{MO}_{x+1}$ , the electrocatalytic activity of *subnon-active* anodes does not provide enough adsorption sites, in the same way as BDD. However, BDD possesses a wide electrochemical window, approximately +2.5 V vs. RHE [52], which is advantageous because the oxygen evolution reaction (Equation 22) occurs above that potential. This characteristic also gives BDD the capacity to form possible reactive oxidants such as ozone and hydrogen peroxide, contrary to *subnon-active* anodes, where the oxygen evolution potential competes with the side mineralization reaction because of their small electrochemical window. In this way, BDD electrodes are the most suitable anodes for mineralizing organic compounds.

#### 4. CONCLUSIONS

The synthesis and characterization of DSAs composed of  $\text{Ti}|\text{IrO}_2\text{-SnO}_2\text{-Sb}_2\text{O}_3$  were successfully achieved by a modified Pechini method using chloride-free precursors. Due to the absence of this ion, the electrode manufacturing process does not produce chlorine vapors, which means that this coating method is environmentally friendly. Physical characterization showed that  $\text{SnO}_2\text{-IrO}_2\text{-Sb}_2\text{O}_3$  films were thermally formed on the Ti substrate from organic compounds as metallic precursors. With this novel method, homogeneous films that do not present cracked features at the microscopic level were obtained. The organic precursors used to synthesize the DSAs allowed us to obtain a metal oxide coating with high surface roughness and good mechanical resistance. All synthesized electrodes were able to produce hydroxyl radicals as *non-active* electrodes. However, in this work, we suggest the term “*subnon-active*” to classify these electrodes because they exhibited lower extension of mineralization than the BDD electrodes reported in the literature.

Regarding their performance, all the synthesized electrodes showed similar behavior in tartrazine and dibenzothiophene oxidation. TRZ oxidation in aqueous media occurred mainly by mediated oxidation through  $\bullet\text{OH}$ , while DBT oxidation in organic media was carried out mainly by direct electron transfer with the electrode surface. Ninety percent color removal and 70% mineralization were achieved after 120 min of electrolysis for the TRZ solution, and 80% dibenzothiophene was converted in 90 min. It is important to note that the use of a low concentration of iridium was sufficient to obtain the best degradation percentage of organic compounds. This point represents an advantage because it reduces the associated costs of producing DSAs. Additionally, it is relevant to mention that the relatively high cost of organic precursor salts is compensated by the low quantities needed for preparing the electrodes and the lack of chlorine compounds.

## ACKNOWLEDGEMENTS

The authors acknowledge BUAP for financial support through VIEP projects. U.B.M. acknowledges CONACYT for a scholarship.

## References

1. C. Comninellis, *Electrochim. Acta*, 39 (1994) 1857.
2. B. Correa-Lozano, C. Comninellis and A. Battisti, *J. Appl. Electrochem.*, 27 (1997) 970.
3. Y. Feng and J. Liu, H. Ding in Preparation, analysis and behaviors of Ti-Based SnO<sub>2</sub> electrode and the function of rare-Earth doping in aqueous wastes treatment in *Electrochemistry for The Environment*, (2010) (Eds.: C. Comninellis and G. Chen), Springer, Netherlands.
4. C. Barrera-Díaz, P. Cañizares, F.J. Fernández, R. Natividad and M.A. Rodrigo, *J. Mex. Chem. Soc.*, 58 (2014) 256.
5. C.R. Costa, C.M Botta, E.L.G. Espindola and P. Olivi, *J. Hazard. Mater.*, 153 (2008) 616.
6. M. Moradi, Y. Vasseghian, A. Khataee, M. Kobya, H. Arabzade and E.N. Dragoi, *J. Ind. Eng. Chem.*, 87 (2020) 18.
7. N. Menzel, E. Ortel, K. Mette, R. Kraehnert and P. Strasser. *ASC Catal.*, 3 (2013) 1324.
8. M. Castanho, G.R.P. Malpass and A.J. Motheo, *Appl. Catal., B*, 62 (2006) 193.
9. C. Comninellis and G.P. Vercesi, *J. Appl. Electrochem.*, 21 (1991) 335.
10. J. Ribeiro, M.S. Moats and A.R. de Andrade, *J. Appl. Electrochem.*, 38 (2008) 767.
11. F.A. Rodríguez, E.P. Rivero and I. González, *MethodsX*, 5(2018) 1613.
12. M.P. Pechini, U.S. Patent 3,330,697, 1967.
13. T.L. Luu, J. Kim and J. Yoon, *J. Ind. Eng. Chem.*, 21 (2015) 400.
14. P. Shrivastava and M.S. Moats, *J. Appl. Electrochem.*, 39 (2009) 107.
15. A. de Oliveira-Sousa, M.A.S. da Silva, S.A.S. Machado, L.A. Avaca and P. de Lima-Neto, *Electrochim. Acta*, 45 (2000) 4467.
16. M.O. Santos, G.O.S. Santos, S. Mattedic, S. Grizad, K.I.B. Eguiluz and G.R. Salazar-Banda, *J. Electroanal. Chem.*, 829 (2018) 116.
17. Y. Xu, X. Yuan, G. Huang and H. Long, *Mater. Chem. Phys.*, 90 (2005) 333.
18. N. Anantha, R. Subba and V.T. Venkatarangaiah, *Environ. Sci. Pollut. Res.*, 21 (2014) 3197.
19. B.D. Soni, U.D. Patel, A. Agrawal, J.P. Ruparelia, *J. Water Process Eng.*, 17 (2017) 11.
20. G. Chen, X. Chen and P.L. Yue, *J. Phys. Chem. B*, 106 (2002) 4364.
21. K.L. Meaney and S. Omanovic, *Mater. Chem. Phys.*, 105 (2007) 143.
22. S. Trasatti and O.A. Petrii, *J. Electroanal. Chem.*, 327 (1992) 353.
23. C. Sicard-Roselli, E. Brun, M. Gilles, G. Baldacchino, C. Kelsey, H. McQuaid, C. Polin, N. Wardlow and F. Currell, *Small*, 10 (2014) 3338.
24. E. Méndez, M.A. González-Fuentes, M.M. Dávila and F.J. González, *J. Electroanal. Chem.*, 751 (2015) 7.
25. L.A. da Silva, V.A. Alves, S.C. de Castro and J.F.C. Boodts, *Colloids Surf. A*, 170 (2000) 119.
26. F. Montilla, E. Morallón, A. de Battisti and J.L. Vázquez, *J. Phys. Chem. B*, 108 (2004), 5036.
27. J.C. Forti, P. Olivi and A.R. de Andrade, *Electrochim. Acta*, 47 (2001) 913.
28. R.D. Coteiro, F.S. Teruel, J. Ribeiro and A.R. de Andrade *J. Braz. Chem. Soc.*, 17 (2006) 771.
29. J.Y. Lee, D.K. Kang, K.H. Lee and D.Y. Chang, *Mater. Sci. Appl.*, 2 (2011) 237.
30. M. Galicia and F.J. González, *J. Electrochem. Soc.*, 149 (2002) D46.
31. M.A. González-Fuentes, B.R. Díaz-Sánchez, A. Vela and F.J. González, *J. Electroanal. Chem.*, 670 (2012) 30.
32. A.S. Pronin, S.A. Semenov, D.V. Volchova and G.I. Dzhardimalieva, *Russ. J. Inorg. Chem.*, 65 (2020) 1173.
33. F.O. Rice and W.R. Johnston, *J. Am. Chem. Soc.*, 56 (1934) 214.

34. M.H.P. Santana, L.A. De Faria and J.F.C. Boodts, *Electrochim. Acta*, 49 (2004) 1925.
35. S. Fierro, A. Kapalka and C. Comninellis, *Electrochem. Commun.*, 12 (2010) 172.
36. H. Czili and A. Horváth, *Appl. Catal. B*, 8 (2008) 295.
37. N.L. Wu, J.Y. Hwang, P.Y. Liu, C.Y. Han, S.L. Kuo, K.H. Liao, M.H. Lee and S.Y. Wang, *J. Electrochem. Soc.*, 148 (2001) A550.
38. Y.J. Liu, C.Y. Hu and S.L. Lo, *J. Hazard. Mater.*, 366 (2019) 592.
39. A. Thiam, M. Zhou, E. Brillas and I. Sirés, *Appl. Catal. B*, 150-151 (2014) 116.
40. L.M. Santos, K.P. de-Amorim, L.S. Andrade, P.S. Batista, A.G. Trovó and A.E.H. Machado, *J. Braz. Chem. Soc.*, 26 (2015) 1817.
41. C. Zhang, G. Ren, W. Wang, X. Yu, F. Yu, Q. Zhang and M. Zhou, *Sep. Purif. Technol.*, 208 (2019) 76.
42. G.H. Abdullah and Y. Xing, *Energy Fuels*, 32 (2018) 8254.
43. E. Brillas, I. Sirés and M.A. Oturan, *Chem. Rev.*, 109 (2009) 6570.
44. A. Thiam, M. Zhou, E. Brillas and I. Sirés, *J. Chem. Technol. Biotechnol.*, 89 (2014) 1136.
45. J.L. Nava, F. Nuñez and I. González, *Electrochim. Acta*, 52 (2007) 3229.
46. A.J. dos Santos, I. Sirés, C.A. Martínez-Huitle and E. Brillas, *Chemosphere*, 210 (2018) 1137.
47. S. García-Segura, A. El-Ghenymy, F. Centellas, R.M. Rodríguez, C. Arias, J.A. Garrido, P.L. Cabot and E. Brillas, *J. Electroanal. Chem.*, 681 (2012) 36.
48. M. Panizza and G. Cerisola, *Chem. Rev.*, 109 (2009) 6541.
49. J.L.S. Duarte, L. Meili, L.M. Gomes, J.M.O. Melo, A.B. Ferro, M.G. Tavares, J. Tonholo and C.L.P.S. Zanta, *Chem. Eng. Process.*, 142 (2019) 107548.
50. C.A. Martínez-Huitle and L.S. Andrade, *Quim. Nova*, 34 (2011) 850.
51. B. Adams and M. Tian, A. Chen, *Electrochim. Acta*, 54 (2009) 1491.
52. F. Montilla, A. Gamero–Quijano and E. Morallón, *Bol. Grupo Español Carbón*, 31 (2014) 8.